

Elemental Nanoanalysis of Interfacial Alumina–Aryl Fluoride Interactions in Fullerene-Free Organic Tandem Solar Cells

Sebastian F. Hoefler, Georg Haberfehlner, Thomas Rath,* Roberto Canteri, Mario Barozzi, Ferdinand Hofer, and Gregor Trimmel*

The choice of the optimum combination of materials for the absorber layers, electrodes, as well as interfacial layers is highly important to enhance further advances in the field of organic photovoltaics. Usually, these materials are assumed to be stable under the applied processing steps for the fabrication of the solar cells. Herein, organic tandem solar cells are examined with fluorine-containing absorber layers consisting of the fluorinated polymer donor PTB7-Th and the indacenodithiophene-type small molecule acceptor O-IDTBR and MoO₃/Al/PFN-Br as recombination layer. Although both subcells comprise the same low bandgap absorber materials, the tandem solar cells reveal high open-circuit voltage values approaching 2 V. However, using a combination of scanning transmission electron microscopy nanoanalysis techniques and secondary ion mass spectrometry with depth profiling, an unexpected phenomenon is disclosed. It is found that significant amounts of fluorine are accumulated in the recombination layer region which originates very likely from alumina–aryl fluoride interactions responsible for a partial defluorination of the conjugated polymer in the absorber layer.

to overcome various inherent shortcomings of fullerene-based materials, for example, in terms of functionalization, optical absorption behavior, and production costs.^[3–5] The development of novel acceptors by rational molecular design and synthesis of new sophisticated organic semiconductors offers a huge structural variety of electron acceptor materials with tunable optoelectronic properties, excellent charge transport characteristics, and variable energy levels.^[4–9]

Fluorination of conjugated polymers and nonfullerene acceptors is an effective strategy to modify the intrinsic material properties such as optical absorption, charge carrier mobility, and energy levels without introducing steric hindrance to the conjugated backbone.^[10,11] For example, the fluorination leads to a downshift of the highest occupied molecular orbital (HOMO) and the lowest unoccupied molecular orbital (LUMO) energy

levels due to the electron accepting properties of the fluorine moiety.^[10,11] Fluorinated acceptor materials have the advantage of an improved driving force for exciton splitting due to the enhanced LUMO_{donor}–LUMO_{acceptor} energy offset, while the fluorination of the donor species results in increased open-circuit voltage (V_{OC}) values arising from the higher energy offset between the LUMO_{acceptor} and HOMO_{donor} energy levels.

Beside the chemical modification of the absorber materials, the device architecture plays a key role to improve the device performance. In this regard, tandem solar cells exhibit a great potential to further advance the performance of organic photovoltaics (OPV) and benefit from the use of absorber materials with complementary absorption properties in the front and rear subcells in order to utilize the solar irradiation spectrum more efficiently.^[12,13] Moreover, high photovoltages can be obtained in series-connected tandem solar cells with V_{OC} values already exceeding 2 V.^[14] Photovoltaic devices with high V_{OC} values are especially interesting for a wide range of applications, for example, in the field of solar-to-fuel research (e.g., photoelectrochemical water-splitting for hydrogen production)^[14–16] or in combination with electrochemical energy storage devices such as lithium-ion batteries for hybrid energy conversion and storage systems (e.g., photorechargeable batteries).^[17]

Only recently, tandem solar cells with efficiencies of over 17% have been reported.^[18] The photovoltaic performance of tandem solar cells is crucially dependent on the intermediate or recombination layer between the two absorber layers. Various

1. Introduction


Fullerene-free organic solar cells based on donor polymers and small molecular nonfullerene acceptors have been demonstrated to be a viable alternative to fullerene-based analogs with power conversion efficiency (PCE) values exceeding 15%.^[1,2] Solution-processable n-type electron acceptors have considerable advantages

Dr. S. F. Hoefler, Dr. T. Rath, Prof. G. Trimmel
 Institute for Chemistry and Technology of Materials (ICTM)
 NAWI Graz

Graz University of Technology
 Stremayrgasse 9, 8010 Graz, Austria
 E-mail: thomas.rath@tugraz.at; gregor.trimmel@tugraz.at

Dr. G. Haberfehlner, Prof. F. Hofer
 Institute of Electron Microscopy and Nanoanalysis
 Graz University of Technology
 Steyrergasse 17, 8010 Graz, Austria

Dr. R. Canteri, Dr. M. Barozzi
 Fondazione Bruno Kessler - Center for Materials and Microsystems
 Via Sommarive 18, 38123 Povo (Trento), Italy

 The ORCID identification number(s) for the author(s) of this article can be found under <https://doi.org/10.1002/admi.201901053>.

© 2019 The Authors. Published by WILEY-VCH Verlag GmbH & Co. KGaA, Weinheim. This is an open access article under the terms of the Creative Commons Attribution License, which permits use, distribution and reproduction in any medium, provided the original work is properly cited.

DOI: 10.1002/admi.201901053

requirements need to be met by the recombination layer such as a high optical transparency to reduce optical losses, a good solvent resistivity to protect the front subcell from damage during processing of the rear subcell, and efficient electron–hole recombination at the intermediate layer, which is critically important for high photocurrent generation and thus the overall solar cell performance.^[19] Various intermediate layer combinations prepared using solution- or vacuum-based deposition methods have been examined in tandem solar cells including metals (e.g., aluminum,^[16] silver,^[20] gold^[21]), metal oxides (e.g., MoO₃,^[20,22] ZnO^[14,22–25]), polymers (e.g., PEDOT:PSS,^[14,24,26] PCP-Na^[23]), polyelectrolytes (e.g., PFN,^[20] PFN-Br,^[27] CPEPh-Na^[25]), or materials such as Bphen^[28] or titanium (diisopropoxide) bis(2,4-pentanedionate).^[29] Among them, aluminum-based intermediate layers showed an excellent performance in combination with metal oxides (e.g., MoO₃/Al,^[30] MoO₃/Al/ZnO^[16]), and are therefore often used in organic tandem solar cells. In addition, aluminum is commonly used as low-work function top electrode contact in both tandem solar cells as well as single-junction solar cells because of the lower material costs and higher abundance in the Earth's crust in comparison to silver or gold electrodes.

Aluminum, however, exhibits a high reactivity and therefore shows miscellaneous effects on the interface with organic semiconductors. For instance, aluminum induces the chemical degradation of fullerene derivatives in organic solar cells, destroying the electron delocalization on the C₆₀ structure.^[31] Aluminum is also reported to diffuse into the organic layer upon thermal evaporation forming a mixed interlayer (≈3 nm) in P3HT:PCBM-based organic solar cells.^[32] In addition, phase segregation effects have been found at the active layer/electrode interface upon thermal deposition, which is accompanied with a modification of the surface composition.^[33] Ling et al. reported the formation of an aluminum oxide interface between the organic semiconductor and the aluminum top contact due to the interaction of aluminum with physically adsorbed oxygen concomitant with the migration of adsorbed oxygen to the surface upon metal deposition.^[34] Moreover, an Al–O–C species was found to be formed at the polymer/metal interface.^[34] This metal–oxygen–carbon interaction has also been reported for a poly(*p*-phenylene vinylene) (PPV)/aluminum system originating from the chemical interaction between the partly oxidized conjugated polymer and the initially formed metal oxide sublayer.^[35]

Therefore, understanding the interactions between adjacent layers in the solar cell stack, in particular interface phenomena upon metal deposition by thermal evaporation is essential since material degradation, intermixing processes, or chemical interactions have a considerable effect on the performance, stability, and lifetime of semiconductor devices.

In this work, we examined the interface effects between the fluorine-containing absorber layer and an aluminum-based recombination layer in fullerene-free organic tandem solar cells. In detail, as absorber material, we used a combination of the fluorinated conjugated polymer PTB7-Th (poly[4,8-bis(5-(2-ethylhexyl)thiophen-2-yl)benzo[1,2-*b*;4,5-*b'*]dithiophene-2,6-diyl-*alt*-(4-(2-ethylhexyl)-3-fluorothieno[3,4-*b*]thiophene-)-2-carboxylate-2,6-diyl)] as donor and the nonfluorinated small molecule acceptor O-IDTBR ((5*Z*,5'*Z*)-5,5'-(((4,4,9,9-tetraoctyl-4,9-dihydro-s-indaceno[1,2-*b*:5,6-*b'*]dithiophene-2,7-diyl)bis(benzo[*c*][1,2,5-

thiadiazole-7,4-diyl))bis(methanylylidene))bis(3-ethyl-2-thioxo-thiazolidin-4-one)).^[36–38] A highly effective metal oxide/metal-based recombination layer was introduced, and polyfluorene-type polyelectrolyte interfacial layers were found to reduce voltage losses, which is favorable for realizing high photovoltage values. In order to investigate the layer stack of the tandem solar cells and the interfaces in detail, scanning transmission electron microscopy (STEM) nanoanalysis with energy dispersive X-ray (EDX) and electron energy loss spectroscopy (EELS) elemental mapping as well as secondary ion mass spectrometry (SIMS) analysis with depth profiling were used.

2. Results and Discussion

PTB7-Th is a high-performance donor–acceptor (D–A) copolymer with a 2D conjugated structure consisting of alternating benzo[1,2-*b*;4,5-*b'*]dithiophene (BDT) and fluorinated thieno[3,4-*b*]thiophene (TT) units, which are used as donor and acceptor building blocks (Figure 1A). The fluorination enhances the electron accepting properties of the TT building block due to the electron withdrawing nature of fluorine and thus causes a downshift of the HOMO energy level (–5.24 eV^[36]) with respect to the nonfluorinated derivative (–5.09 eV for PBDTTT-E-T^[39]). The nonfullerene acceptor O-IDTBR has an acceptor–donor–acceptor (A–D–A) structure consisting of an electron-donating indaceno[1,2-*b*:5,6-*b'*]dithiophene core, flanked by two benzothiadiazole moieties and two electron-withdrawing rhodanine terminal groups (Figure 1A). The photovoltaic properties of this donor:acceptor blend, especially in regard to the molar weight dependence of the donor polymer, has been recently studied in detail.^[38] A discussion on the optical properties and photovoltaic characteristics of the single-junction solar cells is provided in the Supporting Information.

In order to determine the photovoltaic performance, single-junction solar cells were fabricated and optimized in inverted, bulk-heterojunction-type architecture (Figure S2, Supporting Information), consisting of glass/indium tin oxide (ITO, ≈130–140 nm)/ZnO (≈30–40 nm)/PTB7-Th:O-IDTBR (≈80–90 nm)/MoO₃ (10 nm)/Ag (100 nm) using PTB7-Th and O-IDTBR as donor and acceptor species, respectively. The active layer thickness is known to be a decisive parameter to optimize the device performance of organic solar cells and was varied in the range of about 65–95 nm, exhibiting an optimum at 85 ± 4 nm (Figure S3, Supporting Information). The best-performing device has a V_{OC} of 0.99 V, a J_{SC} of 16.0 mA cm^{–2}, a fill factor (FF) of 64.5%, and an efficiency of 10.2%, as shown in Figure S4 in the Supporting Information. This is among the highest PCE values for fullerene-free organic solar cells in inverted architecture using either PTB7-Th^[38,40–43] or O-IDTBR.^[37,44–46]

Due to the remarkably high V_{OC} values (≈1.00 V) together with the high photovoltaic performance above 10%, the examined PTB7-Th:O-IDTBR system is an excellent candidate for the preparation of high open-circuit voltage tandem solar cells. In a first step, organic homo-tandem solar cells were studied in inverted architecture consisting of glass/ITO (≈130–140 nm)/ZnO (≈30–40 nm)/PTB7-Th:O-IDTBR/intermediate layer/PTB7-Th:O-IDTBR/MoO₃ (10 nm)/Ag (100 nm), as schematically shown in Figure 1B and in the cross-sectional scanning

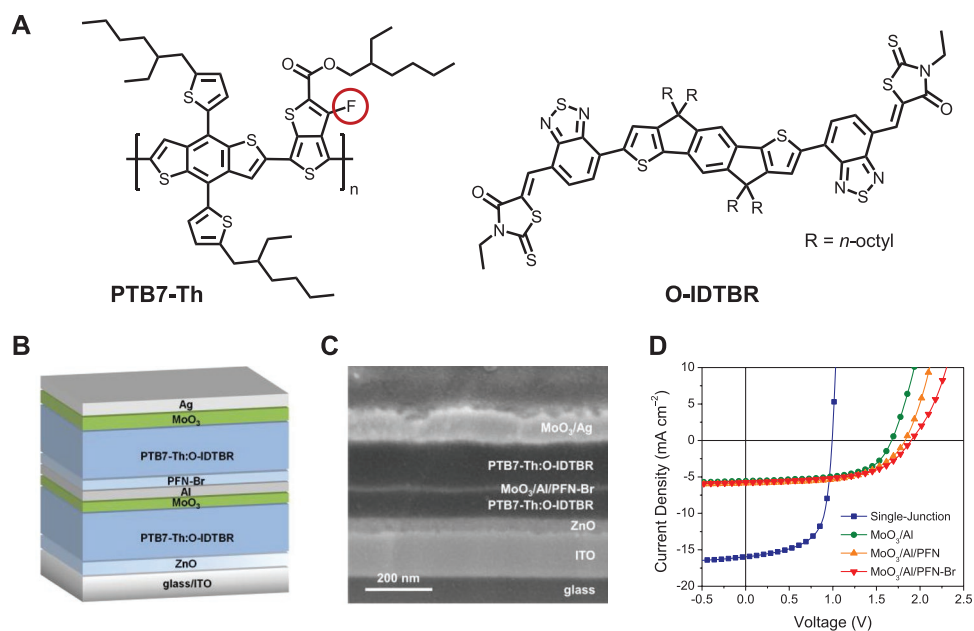


Figure 1. A) Chemical structures of PTB7-Th and O-IDTBR. B) Schematic representation and C) a cross-sectional SEM image of a PTB7-Th:O-IDTBR-based organic homo-tandem solar cell in inverted device architecture with a MoO₃/Al/PFN-Br recombination layer. D) *J*–*V* curves of PTB7-Th:O-IDTBR single-junction and homo-tandem solar cells with different recombination layers under illumination.

electron microscope (SEM) image (Figure 1C). In order to reduce the voltage loss and to achieve high photovoltages, various intermediate layer combinations were examined. **Table 1** summarizes the photovoltaic performance parameters averaged over five individual devices with different recombination layers, while the current density–voltage (*J*–*V*) curves are shown in Figure 1D. Using MoO₃ (8 nm)/Al (3 nm) as intermediate layer, the *V*_{OC} was significantly improved from 0.99 V (single-junction) to 1.67 ± 0.02 V. However, due to the similar absorption properties of the front and the rear subcell, the *J*_{SC} values significantly decreased (5.3 ± 0.2 mA cm⁻²) compared to the single-junction reference solar cells (15.9 ± 0.2 mA cm⁻²), which caused a substantial decrease of the PCE values from 10.01 ± 0.12% to 5.05 ± 0.26%.

This recombination layer could be improved by the addition of ultrathin films of conjugated polyfluorene-type polyelectrolytes such as PFN (poly[(9,9-bis(3'-(*N,N*-dimethylamino)propyl)-2,7-fluorene)-*alt*-2,7-(9,9-dioctylfluorene)]) and PFN-Br (poly[(9,9-bis(3'-(*N,N*-dimethyl)-*N*-ethylammonium)-propyl)-2,7-fluorene)-*alt*-2,7-(9,9-dioctylfluorene)]) dibromide) to the

MoO₃/Al-based intermediate layer. The incorporation of such an ultrathin polyelectrolyte layer between the recombination layer and the active layer of the rear subcell was reported to reduce the work function of MoO₃/metal intermediate layers induced by the formation of interfacial dipoles, which is favorable to improve the solar cell performance.^[15,20,47,48] Accordingly, the incorporation of an ultrathin PFN interlayer (<5 nm) enhanced the *V*_{OC} value further to 1.79 ± 0.05 V, corresponding to only a small voltage loss of ≈10% based on Kirchhoff's law. This is accompanied by slightly improved *J*_{SC} values (5.8 ± 0.1 mA cm⁻²) and PCE values (5.85 ± 0.14%). By substituting the neutral polymer PFN with its cationic derivative PFN-Br, remarkably high *V*_{OC} values up to 1.92 V were obtained, which is among the highest values reported for organic tandem solar cells.^[14,15,23,49] The *V*_{OC} of the organic tandem solar cells is almost equal to the sum of the individual subcells, showing only a small voltage loss of about 60 mV, which corresponds to a loss of about 3% according to Kirchhoff's law. These *V*_{OC} values are outstanding for a system which is entirely based on low bandgap donor and acceptor materials, and are significantly

Table 1. Photovoltaic performance parameters of PTB7-Th:O-IDTBR organic homo-tandem solar cells with different intermediate layers.

Intermediate layer	<i>V</i> _{OC} [V]	<i>J</i> _{SC} [mA cm ⁻²]	FF [%]	PCE [%]
Single-junction	0.99	15.9 ± 0.2	63.7 ± 0.8	10.01 ± 0.12 (max. 10.19)
MoO ₃ /Al	1.67 ± 0.02	5.3 ± 0.2	58.6 ± 1.8	5.05 ± 0.26 (max. 5.42)
MoO ₃ /Al/PFN	1.79 ± 0.05	5.8 ± 0.1	56.8 ± 0.9	5.85 ± 0.14 (max. 6.05)
MoO ₃ /Al/PFN-Br	1.90 ± 0.02	5.7 ± 0.1	56.7 ± 0.6	6.03 ± 0.06 (max. 6.10)
MoO ₃ /Al/PFN-Br ^a (70/120 nm)	1.92 ± 0.02	6.6 ± 0.2	54.2 ± 0.6	6.79 ± 0.15 (max. 7.01)

^aParameters were extracted from *J*–*V* curves under illumination without a shadow mask (active electrode area: 9 mm²). The values in parenthesis represent the optimized layer thickness of the front and rear subcell.

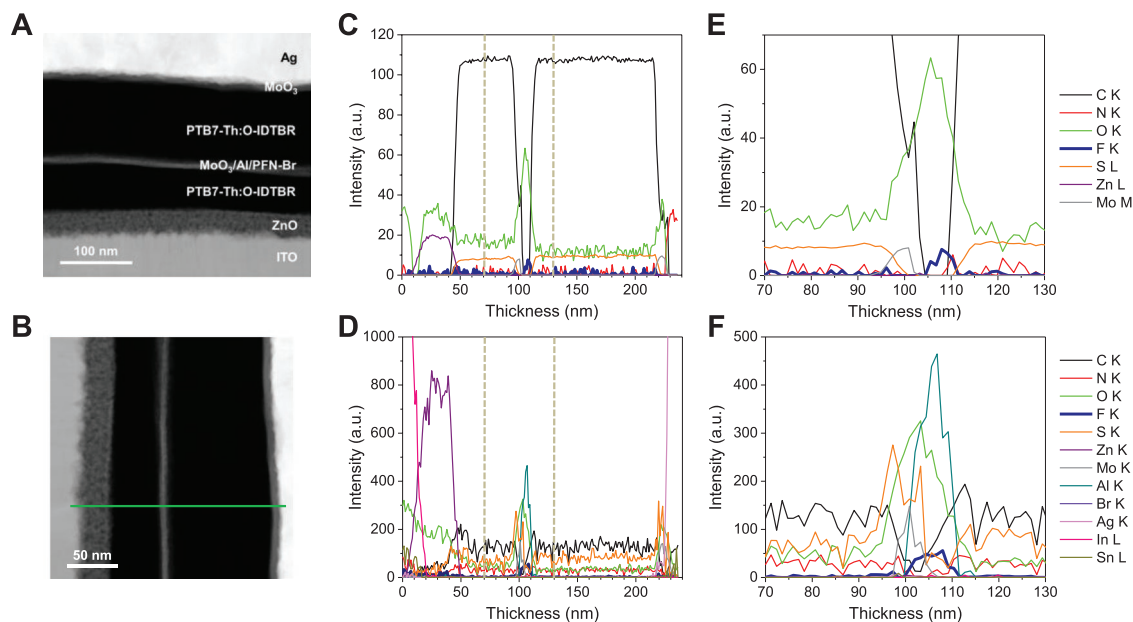


Figure 2. Cross-sectional STEM HAADF image of an FIB prepared lamella of A) a PTB7-Th:O-IDTBR-based organic tandem solar cell. B) STEM HAADF image of the tandem solar cell (the green line indicates the position of the line scan used for the analysis of the elemental distributions) and the corresponding C) EELS and D) EDS elemental distribution mapping for the photovoltaic device and the intermediate layer region (E: EELS, F: EDS).

higher compared to PTB7-Th:PC₇₁BM homo-tandem solar cells ($\approx 1.5\text{--}1.6$ V).^[25,26] Due to the considerable improvement of the V_{OC} , the efficiency of the organic tandem solar cells could be further improved to over 6% ($6.03 \pm 0.06\%$), demonstrating the potential of the MoO₃/Al/PFN-Br intermediate layer as efficient electron–hole recombination site in polymer:small molecule organic tandem solar cells.

The photovoltaic performance is, however, still limited by low J_{SC} values (≈ 5.8 mA cm⁻²), which can be explained by nonoptimized layer thicknesses of the active layers within the front and the rear subcells, i.e., the photocurrent generation of the rear subcell is limited by the high absorption of the front subcell. In addition, the mismatched photocurrents might cause charge carrier accumulation in the subcells, which increases recombination losses and therefore reduces FF values.^[14,50] In order to overcome these issues, the active layer thicknesses of the front and rear subcells were thoroughly optimized (Table S2, Supporting Information). The J – V curves and the photovoltaic performance parameters for different active layer thickness combinations are shown in Figures S5 and S6 in the Supporting Information. The J_{SC} values could be slightly improved by optimizing the layer thickness of the front subcell (60–70 nm), which correlates with the local maximum found for single-junction solar cells (Figure S3, Supporting Information), and the rear subcell (120–130 nm). The higher J_{SC} values correlate well with the enhanced FF values, indicating a lower series resistance in the solar cells. As a consequence, the best-performing device was obtained for a layer thickness combination of 70/120 nm (front/rear subcell), exhibiting a V_{OC} of 1.94 V, a J_{SC} of 6.89 mA cm⁻², an FF of 53.5%, and an efficiency of 7.01% ($6.79 \pm 0.15\%$). External quantum efficiency (EQE) spectra of a single-junction and a tandem solar cell with a MoO₃/Al/PFN-Br intermediate layer are depicted in Figure S7 in the Supporting Information. The EQE spectrum of the tandem solar cell shows a minimum

between 630 and 700 nm, the wavelength region, in which the single-junction solar cell shows the highest EQE values. This suggests that the front subcell in these homo-tandem solar cells is still too thick. However, a further reduction of the front subcell thickness to values under 60 nm led to significantly reduced voltages in the single-junction as well as the tandem solar cells.

Figure 2A shows a cross-sectional scanning transmission electron microscopy high-angle annular dark-field (HAADF) image of a focused ion beam (FIB) prepared lamella of such an organic tandem solar cell. The individual layers comprising ITO/ZnO/absorber layer/intermediate layer/absorber layer/electrode can be clearly distinguished, implying that the MoO₃/Al/PFN-Br recombination layer is robust enough to effectively protect the front subcell from damage during the solution processing of the rear subcell. Based on electron microscopy and surface profilometry, the thicknesses of the individual layers are: ITO ($\approx 130\text{--}140$ nm), ZnO ($\approx 30\text{--}40$ nm), PTB7-Th:O-IDTBR ($\approx 55\text{--}70$ nm front subcell, $\approx 110\text{--}120$ nm rear subcell), intermediate layer (≈ 15 nm), MoO₃ (10 nm), and Ag (100 nm).

STEM nanoanalysis measurements were performed to elucidate the chemical composition of each layer. A special focus was set on interface effects between the individual layers in the multilayer system, especially with regard to the interaction between the solution-processed layers (e.g., absorber layers, interfacial layers) and the thermally evaporated compounds (e.g., intermediate layers). From the line scan of the cross-sectional STEM HAADF image (Figure 2B), the elemental distribution throughout the photovoltaic device was determined via electron energy loss spectroscopy and via energy dispersive X-ray spectroscopy (EDS). As shown in the EELS and EDS elemental nanoanalysis (Figure 2C–F), the elemental composition of carbon (C K), oxygen (O K), and sulfur (S K, S L) in the active layer region of the front and rear subcell remains constant, indicating a proper mixing of the polymer donor and

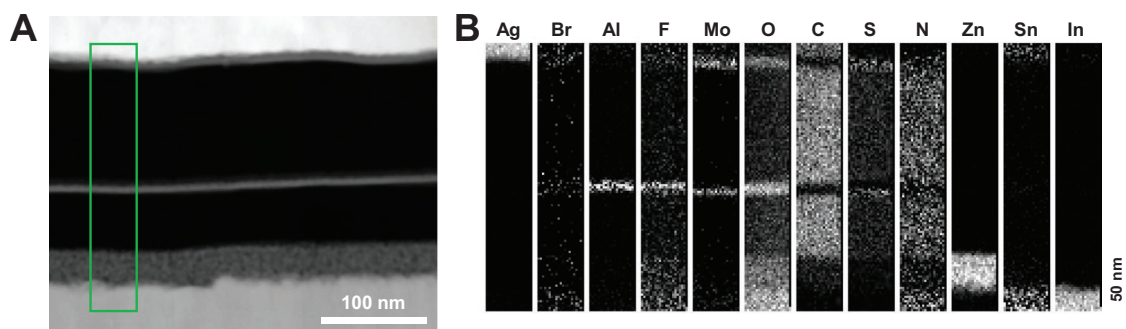


Figure 3. A) Cross-sectional STEM HAADF image of a FIB prepared lamella of a PTB7-Th:O-IDTBR-based organic tandem solar cell (with the position of the spectrum image indicated), and B) the corresponding EDS elemental distribution images.

the small molecule acceptor and no macroscopic segregation or gradient of one of the components. In addition, a signal for nitrogen (N K, from O-IDTBR) and a very weak signal for fluorine (F K, from PTB7-Th) can be found. Molybdenum (Mo K, Mo M) was detected in the intermediate layer region as well as between the absorber layer of the rear subcell and the silver top electrode (Ag K), and correlates with the signal for oxygen (O K), implying the presence of the molybdenum(VI) oxide (MoO_3) interlayers. In addition, a distinct increase of the aluminum signal (Al K) was found in the region of the intermediate layer in the EDS line scan together with an intense oxygen (O K) signal, implying the formation of aluminum oxide. Oxygen (O K) was also found in the ZnO layer (together with zinc (Zn K, Zn L)) and within the ITO layer (together with indium (In L) and tin (Sn L)). The presence of an ultrathin PFN-Br interfacial layer is indicated by a small shoulder of the carbon and nitrogen signals; however, bromine (Br K) could not be found, which might be related to the low absolute concentration of bromide (layer thickness below 5 nm) and relatively weak ionic bonding to the polycationic species. Surprisingly, a relatively high amount of fluorine was detected in the intermediate layer region located between the MoO_3 layer and the PFN-Br layer even though no fluorinated compounds were used within the recombination layer. Even more, the detected amount was even higher than in the absorber layer, where fluorine is expected to be present due to the fluorinated polymer PTB7-Th.

Unraveling the reason for the presence of fluorine within the intermediate layer, all the individual compounds (PFN-Br, MoO_3 , aluminum) were examined separately via scanning electron microscopy and STEM measurements combined with EDX and EELS elemental analysis. However, no fluorine was detected in the materials and, therefore, any contamination from the processing methodology or impurities of the chemicals can be excluded (Figures S8–S10, Supporting Information). In addition, a fluorine-free reference system was examined using P3HT (poly(3-hexylthiophene-2,5-diyl)) and O-IDTBR as donor and acceptor materials for the absorber layer and the same device configuration (Figure S11, Supporting Information). All other process parameters—especially the solvents—were kept constant and only PTB7-Th was substituted with the nonfluorinated polymer P3HT. However, no fluorine was found in this reference system and thus contamination from the processing methodology or impurities from the solvent can be excluded. Therefore, the only conclusive explanation is

that the fluorine found in the recombination layer of the PTB7-Th:O-IDTBR tandem solar cells derives from the fluorinated TT moiety of the conjugated polymer. Moreover, even though fluorine is accumulated in the region of the intermediate layer, no significant amounts of carbon and sulfur were found in this area of the device (Figure 3), which should be present if the polymer is accumulated at the interface and the chemical structure of PTB7-Th would be still intact, implying that the polymer is partially decomposed or fragmented.

Having a closer look at the element distributions in the intermediate layer (Figure 3; Figure S12, Supporting Information), it is evident that the fluorine signal correlates with enhanced amounts of aluminum and oxygen, originating from the formation of alumina most probably due to the thermal evaporation process of aluminum under high vacuum conditions ($\approx 10^{-5}$ mbar) and the reaction with MoO_3 and/or surface adsorbed oxygen.^[31,34] Interestingly, no fluorine is detected within the region of the MoO_3 film. This leads to the assumption that alumina plays an important role in the accumulation of fluorine in the intermediate layer. The low concentrations of fluorine as well as nitrogen detected in the region of the ITO layer originate from contributions to the signal stemming from bremsstrahlung X-rays, which can influence the results for very light elements.

These data lead to the hypothesis that the fluorine substituent is dissociated from the aromatic TT unit of the conjugated polymer even though the C–F bond is typically more stable compared to the C–C bond. However, aromatic C–F bond activation via alumina-mediated processes—although only at elevated temperatures—has already been reported in the literature,^[51] which underlines the feasibility of the proposed dissociation mechanism of fluorine.

In order to investigate if the accumulation of fluorine is solely limited to aluminum-containing recombination layers, additional metals (Ag and Au) commonly used within recombination layers as well as electrode materials were evaluated. Therefore, a multilayer comprising PTB7-Th:O-IDTBR absorber layers together with $\text{MoO}_3/\text{Al}/\text{PFN-Br}$, $\text{MoO}_3/\text{Au}/\text{PFN-Br}$, and $\text{MoO}_3/\text{Ag}/\text{PFN-Br}$ intermediate layers was examined via STEM EDX nanoanalysis (Figure S13, Supporting Information). Fluorine was found again in relatively high amounts in the region of the aluminum/alumina layer. Within the gold- and silver-containing recombination layers, which form large cluster-like particles, the fluorine signal is considerably lower. The differences

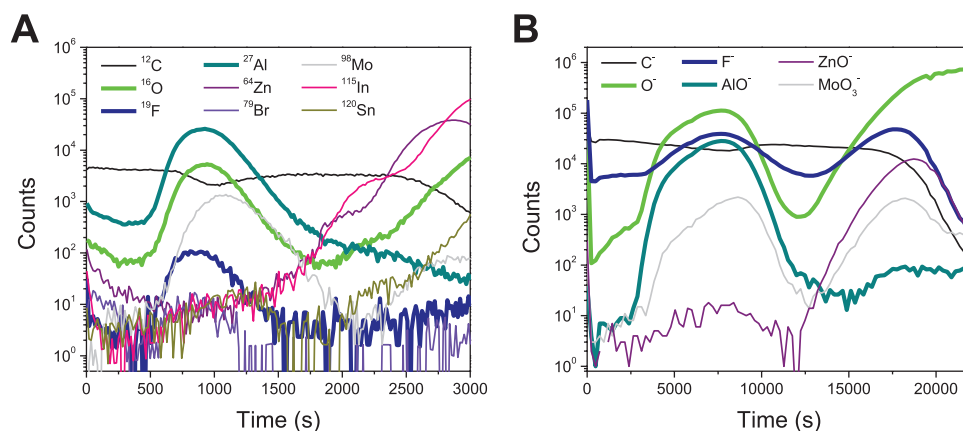


Figure 4. A) D-SIMS depth profiling. The acquisition was done using the MCs⁺ technique implying that the detected species were CCs⁺, OCs⁺, FCs⁺, etc. For clarity, they are denoted as ¹²C, ¹⁶O, ¹⁹F, etc. in the graph. B) Depth profiling data based on ToF-SIMS measurements performed in negative mode.

with regard to the fluorine accumulation might be related to the oxidation of aluminum upon thermal evaporation, which is not the case for silver and gold due to the rather inert nature of the metals and higher stability. This is in good agreement with the data reported in the literature.^[31,33]

In addition, to verify the presence of fluorine in the intermediate layer with an independent method, depth profiling with dynamic secondary ion mass spectrometry (D-SIMS) and time-of-flight secondary ion mass spectrometry (ToF-SIMS) was performed (Figure 4). D-SIMS offers a very high depth resolution and is less affected by matrix effects than ToF-SIMS, which was additionally applied to support the D-SIMS results and to possibly obtain further information on the chemical nature of the fluorine found within the recombination layer. For these experiments, a multilayer film without a MoO₃/Ag top contact was fabricated (Figure S14, Supporting Information) to avoid an extensive smearing effect which would complicate the analysis of the depth profiling experiment. Figure 4A shows increased concentrations of ²⁷Al, ¹⁶O, ¹⁹F, ⁷⁹Br, and ⁹⁸Mo in the intermediate layer region (at a sputtering time between ≈600 and 1400 s). In accordance with the sample architecture, the maximum of the ⁷⁹Br peak, originating from the PFN-Br polyelectrolyte interfacial layer, appears at a slightly lower sputtering time compared to the other elements present in the recombination layer. It should be noted that the PFN-Br layer has only been detected in the SIMS analysis and could not be observed in the STEM nanoanalysis due to the different detection limits of both techniques. At slightly higher sputtering time, the maxima of the ²⁷Al and the ¹⁹F peak are detected at the same position, followed by the maximum of the ⁹⁸Mo peak. Based on this observation, we can confirm i) an increased concentration of fluorine in the intermediate layer and ii) its localization within or in closest proximity to the alumina layer, which supports the above discussed electron microscopic results. The increased ⁹⁸Mo signal in the region of the ZnO electron transport layer is most likely due to an overlap of the ⁹⁸Mo peak with one isotope of the ZnO₂-molecule formed during the analysis.

As expected, the peaks appear broader and more smeared in the ToF-SIMS depth profiling (Figure 4B). Interestingly, in contrast to the D-SIMS data, increased amounts of F⁻ are found in the intermediate layer and additionally at the interface

to the ZnO layer due to the higher sensitivity in negative ion polarity mode of the ToF-SIMS measurements. ToF-SIMS is, however, also more prone to matrix effects, which makes it difficult to draw conclusions about the actual concentration of F⁻ at the interface to the ZnO layer, but the presence of slightly increased amounts of F⁻ in this region of the multilayer stack is also corroborated by the EDS elemental distribution images (Figure 3B). In any case, still the highest concentration of F⁻ is found in the intermediate layer. In the region of the intermediate layer, also an AlO⁻ signal was detected due to the formation of alumina. As already known from the electron microscopic elemental mappings, this peak also correlates with the F⁻ signal, implying the interaction of the Al–O species with fluorine. This further supports our hypothesis of a chemical interaction between the alumina species and the fluorine of PTB7-Th via an alumina-mediated aromatic C–F bond activation causing a C–F bond cleavage.^[52,53] Even though such reactions are typically performed at elevated temperatures and/or vacuum conditions (e.g., 100–250 °C^[51–53]), C–F bond activation via alumina-mediated processes have also been reported to proceed at room temperature, however, with considerably lower yields.^[54] Therefore, it is likely that these reactions also occur, e.g., during the thermal evaporation steps in the tandem solar cell fabrication.

The reaction between alumina and fluorine is thus supposed to proceed in analogy to the above mentioned literature reports. It is expected that the ultrathin alumina layer contains reactive sites for the C–F bond activation, which are described as frustrated Lewis acid–base pairs, leading to the dissociation of aromatic C–F bonds.^[54] The activation of the C–F bond is reported to proceed via the coordination of fluorine on the aluminum oxide surface, with the driving force being the Al–F bond formation.^[52–54] In the investigated tandem solar cells, we assume that this defluorination of the conjugated polymer leads to an accumulation of fluorine in the intermediate layer region due to diffusion phenomena of the fragmented species in the multilayer system.

The alumina-mediated dissociation of fluorine from the conjugated polymer is expected to influence device performance and lifetime as the composition of the materials within the absorber layer is altered. Additionally, the changes in the

composition of the interlayer will also modify the relative energy levels or work functions and will influence the band alignment at the interface, and thereby an effect, positive or negative, on the electronic properties of the intermediate layer cannot be excluded. This reaction of organic aryl fluorides with aluminum is of high importance for organic electronic devices, in particular for organic solar cells, since low-work function metals like aluminum are commonly employed as electrode material or as recombination layer in tandem solar cells together with fluorinated materials (polymers like PffBT4T-2OD,^[55] PBDB-T-2F,^[56] or PBDB-T-SF^[57] or nonfullerene acceptors such as ITIC-F,^[57] IEICO-4F,^[58] or CO₈DFIC^[59]) because of its low material costs and the good device performance. Indeed, a first TEM-EDX analysis of a device containing the fluorinated acceptor ITIC-F in combination with the nonfluorinated donor polymer PBDB-T and a MoO₃/aluminum back electrode also shows a similar accumulation of fluorine within an AlO_x layer as shown in Figure S15 in the Supporting Information. Thus, this alumina-aryl fluoride interaction seems to be of general concern in organic electronics.

Therefore, a deeper understanding and further investigations of the influence of this oxygen–metal–fluorine interaction on the device properties is critically important to enhance the progress in the field of organic photovoltaics.

3. Conclusion

Although modern OPV materials are usually stable during the solar cell fabrication steps, unexpected chemical reactions at the interfaces have to be considered in the final device, in particular, if reactive metal interlayers are employed. These interfacial processes are usually hardly detectable by routine solar cell analysis. Thus, we have used a set of elaborated electron microscopy methods (STEM in combination with EDX and EELS) and SIMS-based depth profiling measurements in order to study interface phenomena and elemental distributions in fullerene-free organic tandem cells. We have shown that a fluorine-containing absorber layer in combination with the intermediate layer MoO₃/Al/PFN-Br leads to an accumulation of fluorine in the recombination layer. More precisely, it was found that the fluorine is present in an AlO_x layer. It is suggested that this in situ formed alumina is responsible for the activation of the aromatic C–F bonds in PTB7-Th, causing the dissociation of the C–F bond.

Despite this defluorination reaction, the MoO₃/Al/PFN-Br system is a highly effective recombination layer with only minimal voltage losses (≈60 mV) and remarkably high V_{OC} values (≈1.92 V) in the investigated fullerene-free organic homotandem solar cells using PTB7-Th:O-IDTBR as absorber layer. Thus, this reaction which at least leads to a chemical modification of the polymer structure if not even to a partial degradation, does not seem to harm the functionality of the solar cell. Further investigation and understanding of this interface phenomenon and if this reaction also happens in similar fluorine-containing absorber materials are of utmost importance for the field of organic electronics since a plethora of decisive aspects including material stability, device performance, and lifetime can be affected by these interface phenomena.

4. Experimental Section

Homo-Tandem Solar Cell Fabrication: Prepatterned ITO-coated glass substrates were cleaned by sonication in 2-propanol (60 min, 40–50 °C) and oxygen plasma treatment (3 min, FEMTO, Diener electronic). ZnO thin films were derived from a sol–gel reaction of a zinc oxide precursor solution.^[60] The zinc oxide precursor solution was prepared by dissolving zinc acetate dihydrate (0.5 g, 2.3 mmol) in 2-methoxyethanol (5 mL) using ethanolamine (150 μL, 2.5 mmol) as a stabilizer.^[60] The solution was vigorously stirred overnight under ambient conditions for the hydrolysis reaction, followed by filtration through a 0.45 μm polytetrafluoroethylene (PTFE) syringe filter before spin coating (4000 rpm, 30 s). The ZnO films were annealed under ambient conditions (15 min, 150 °C) to achieve layer thicknesses in the range of 30–40 nm. PTB7-Th was dissolved in *ortho*-dichlorobenzene at 70 °C (12 mg mL⁻¹), blended with O-IDTBR in a donor:acceptor ratio of 1:1.5 by weight (total concentration: 25–30 mg mL⁻¹), and spin-coated to achieve layer thicknesses in the range of 50–80 nm. The intermediate layer was deposited by thermal evaporation of molybdenum(VI) oxide (8 nm, deposition rate: ≈0.1–0.2 Å s⁻¹) and aluminum (3 nm, ≈0.5–1.0 Å s⁻¹). For organic tandem solar cells with the polyelectrolyte interlayer (<5 nm), PFN (2 mg mL⁻¹ in methanol with 2 μL acetic acid mL⁻¹, filtrated through a 0.45 μm polyvinylidene difluoride (PVDF) syringe filter) and PFN-Br (0.5 mg mL⁻¹ in methanol, filtrated through a 0.45 μm PTFE syringe filter) were spin-coated onto the MoO₃/Al intermediate layer. For the rear subcell, PTB7-Th was dissolved in chlorobenzene at 70 °C (9 mg mL⁻¹), blended with O-IDTBR in a donor:acceptor ratio of 1:1.5 by weight (total concentration: 22.5 mg mL⁻¹), and spin-coated to obtain layer thicknesses in the range of 90–140 nm. A molybdenum(VI) oxide anode interfacial layer (10 nm, ≈0.2 Å s⁻¹) and a silver anode (100 nm, 0.1–1.0 Å s⁻¹) were deposited by thermal evaporation under reduced pressure (≈10⁻⁵ mbar) using a shadow mask to define the active area (9 mm²). Additional details are given in the Supporting Information.

Device Characterization: J–V curves were recorded under illuminated and dark conditions in inert atmosphere using a Keithley 2400 source meter, and a Dedolight DLH400D lamp (1000 W m⁻², similar to AM 1.5 G), which was calibrated with a standard reference silicon solar cell (Fraunhofer ISE). The solar cells were illuminated continuously for 5–10 min prior to the measurement of the J–V curves. A metal mask (2.9 × 2.9 mm) was used to define the illuminated electrode area with 8.41 mm² unless otherwise stated. Photovoltaic parameters were determined from the J–V curves under illumination and were averaged over five individual devices.

Scanning Electron Microscopy and Scanning Transmission Electron Microscopy: Cross-sections of the organic tandem solar cells were prepared using a slope-cutter (for SEM), and the FIB technique was performed on an FEI Nova 200 FIB/SEM dual-beam system (for STEM). A platinum protection layer was deposited on the photovoltaic device prior to the FIB preparation of the cross-section. SEM images were acquired on a Zeiss Ultra55 SEM at an acceleration voltage of 3 kV equipped with an in-lens secondary electron detector. STEM images were taken on a probe-corrected FEI Titan³ 60–300 at an acceleration voltage of 300 kV equipped with a Gatan Imaging Filter (GIF) Quantum and a four-quadrant FEI Super-X Silicon Drift Detector. The beam current was ≈150 pA, the convergence angle was 19.6 mrad, and the collection angle for EELS was 20.5 mrad. Both EELS and EDX data were treated in the Gatan Microscopy Suite (GMS) using model-based approaches for the extraction of elemental maps.

Time-of-Flight Secondary Ion Mass Spectrometry and Dynamic Secondary Ion Mass Spectrometry: ToF-SIMS measurements were performed on a ToF-SIMS IV reflectron time-of-flight secondary ion mass spectrometer (IONTOF GmbH) equipped with a bismuth liquid metal ion gun (LMIG). For each sample, negative ion spectra were acquired over an area of 100 μm × 100 μm by using Bi₃⁺ as primary ions with a dose below 10¹² ions cm⁻² to ensure static SIMS conditions. The depth profiles were obtained using a sputtering beam of Xe⁺ at 1000 eV of energy impact to sputter a 300 μm × 300 μm rastered area. After 240 s of sputtering, a full spectrum was acquired. The cycle made by 240 s of sputtering and an

acquisition of spectra was repeated until the interface with the substrate was reached. The D-SIMS measurements were carried out on a Cameca SC-Ultra (CAMECA) equipped with a magnet type mass spectrometer, using Cs⁺ as primary beam and monitoring MCs⁺ secondary molecular ions. The primary ions impact energy was 1 keV and the raster area was 300 μm × 300 μm. The analyzed area, centered on the sputtered area, was 100 μm × 100 μm.

Supporting Information

Supporting Information is available from the Wiley Online Library or from the author.

Acknowledgements

This work was carried out within the project “SolaBat - Solar cell meets battery - Realization of a hybrid energy system” funded by the Austrian “Climate and Energy Fund” within the program Energy Emission Austria (FFG No. 853 627). The support of Ilie Hanzu and Martin Wilkening is gratefully acknowledged. The authors thank Stefan Mitsche, Martina Dienstleder, and Sanja Simic for experimental support regarding the electron microscopic analyses.

Conflict of Interest

The authors declare no conflict of interest.

Keywords

organic electronics, oxygen–metal–fluorine interaction, photovoltaics, scanning transmission electron microscopy, secondary ion mass spectrometry

Received: June 13, 2019

Revised: July 18, 2019

Published online:

- [1] M. A. Green, Y. Hishikawa, E. D. Dunlop, D. H. Levi, J. Hohl-Ebinger, M. Yoshita, A. W. Y. Ho-Baillie, *Prog. Photovoltaics* **2019**, *27*, 3.
- [2] J. Yuan, Y. Zhang, L. Zhou, G. Zhang, H.-L. Yip, T.-K. Lau, X. Lu, C. Zhu, H. Peng, P. A. Johnson, M. Leclerc, Y. Cao, J. Ulanski, Y. Li, Y. Zou, *Joule* **2019**, *3*, 1140.
- [3] S. Zhang, L. Ye, J. Hou, *Adv. Energy Mater.* **2016**, *6*, 1502529.
- [4] C. B. Nielsen, S. Holliday, H.-Y. Chen, S. J. Cryer, I. McCulloch, *Acc. Chem. Res.* **2015**, *48*, 2803.
- [5] W. Chen, Q. Zhang, *J. Mater. Chem. C* **2017**, *5*, 1275.
- [6] N. Liang, W. Jjiang, J. Hou, Z. Wang, *Mater. Chem. Front.* **2017**, *1*, 1291.
- [7] C. Zhan, X. Zhang, J. Yao, *RSC Adv.* **2015**, *5*, 93002.
- [8] Z. Xiao, X. Jia, L. Ding, *Sci. Bull.* **2017**, *62*, 1562.
- [9] L. Liu, Q. Liu, Z. Xiao, S. Yang, Y. Yuan, L. Ding, *Sci. Bull.* **2019**, *64*, 1083.
- [10] Y. Liang, D. Feng, Y. Wu, S.-T. Tsai, G. Li, C. Ray, L. Yu, *J. Am. Chem. Soc.* **2009**, *131*, 7792.
- [11] Q. Zhang, M. A. Kelly, N. Bauer, W. You, *Acc. Chem. Res.* **2017**, *50*, 2401.
- [12] Z. Shi, Y. Bai, X. Chen, R. Zeng, Z. Tan, *Sustainable Energy Fuels* **2019**, *3*, 910.
- [13] Q. Zeng, L. Liu, Z. Xiao, F. Liu, Y. Hua, Y. Yuan, L. Ding, *Sci. Bull.* **2019**, *64*, 885.
- [14] S. Chen, G. Zhang, J. Liu, H. Yao, J. Zhang, T. Ma, Z. Li, H. Yan, *Adv. Mater.* **2017**, *29*, 1604231.
- [15] W. Liu, S. Li, J. Huang, S. Yang, J. Chen, L. Zuo, M. Shi, X. Zhan, C.-Z. Li, H. Chen, *Adv. Mater.* **2016**, *28*, 9729.
- [16] Y. Gao, V. M. Le Corre, A. Gaitis, M. Neophytou, M. A. Hamid, K. Takanabe, P. M. Beaujuge, *Adv. Mater.* **2016**, *28*, 3366.
- [17] H.-D. Um, K.-H. Choi, I. Hwang, S.-H. Kim, K. Seo, S.-Y. Lee, *Energy Environ. Sci.* **2017**, *10*, 931.
- [18] L. Meng, Y. Zhang, X. Wan, C. Li, X. Zhang, Y. Wang, X. Ke, Z. Xiao, L. Ding, R. Xia, H.-L. Yip, Y. Cao, Y. Chen, *Science* **2018**, *361*, 1094.
- [19] T. Ameri, N. Li, C. J. Brabec, *Energy Environ. Sci.* **2013**, *6*, 2390.
- [20] L. Zuo, C.-Y. Chang, C.-C. Chueh, S. Zhang, H. Li, A. K.-Y. Jen, H. Chen, *Energy Environ. Sci.* **2015**, *8*, 1712.
- [21] M. Hiramoto, M. Suezaki, M. Yokoyama, *Chem. Lett.* **1990**, *19*, 327.
- [22] J. You, C.-C. Chen, Z. Hong, K. Yoshimura, K. Ohya, R. Xu, S. Ye, J. Gao, G. Li, Y. Yang, *Adv. Mater.* **2013**, *25*, 3973.
- [23] Y. Cui, H. Yao, B. Gao, Y. Qin, S. Zhang, B. Yang, C. He, B. Xu, J. Hou, *J. Am. Chem. Soc.* **2017**, *139*, 7302.
- [24] C.-C. Chen, W.-H. Chang, K. Yoshimura, K. Ohya, J. You, J. Gao, Z. Hong, Y. Yang, *Adv. Mater.* **2014**, *26*, 5670.
- [25] H. Zhou, Y. Zhang, C.-K. Mai, S. D. Collins, G. C. Bazan, T.-Q. Nguyen, A. J. Heeger, *Adv. Mater.* **2015**, *27*, 1767.
- [26] H. Kang, S. Kee, K. Yu, J. Lee, G. Kim, J. Kim, J. R. Kim, J. Kong, K. Lee, *Adv. Mater.* **2015**, *27*, 1408.
- [27] Z. Shi, H. Liu, J. Li, F. Wang, Y. Bai, X. Bian, B. Zhang, A. Alsaedi, T. Hayat, Z. Tan, *Sol. Energy Mater. Sol. Cells* **2018**, *180*, 1.
- [28] X. Che, X. Xiao, J. D. Zimmerman, D. Fan, S. R. Forrest, *Adv. Energy Mater.* **2014**, *4*, 1400568.
- [29] Z. Shi, H. Liu, L. Xia, Y. Bai, F. Wang, B. Zhang, T. Hayat, A. Alsaedi, Z. Tan, *Chin. J. Chem.* **2018**, *36*, 194.
- [30] D. W. Zhao, X. W. Sun, C. Y. Jiang, A. K. K. Kyaw, G. Q. Lo, D. L. Kwong, *Appl. Phys. Lett.* **2008**, *93*, 083305.
- [31] W. Huang, E. Gann, L. Thomsen, A. Tadich, Y.-B. Cheng, C. R. McNeill, *ACS Appl. Mater. Interfaces* **2016**, *8*, 2247.
- [32] N. Rujisamphan, F. Deng, R. E. Murray, C. Ni, S. Ismat Shah, *Sol. Energy Mater. Sol. Cells* **2013**, *109*, 56.
- [33] I. Dekman, R. Brener, G. L. Frey, *J. Mater. Chem. C* **2013**, *1*, 6522.
- [34] Q. D. Ling, S. Li, E. T. Kang, K. G. Neoh, B. Liu, W. Huang, *Appl. Surf. Sci.* **2002**, *199*, 74.
- [35] T. P. Nguyen, J. L. Mansot, *Thin Solid Films* **1996**, *283*, 135.
- [36] S. Zhang, L. Ye, W. Zhao, D. Liu, H. Yao, J. Hou, *Macromolecules* **2014**, *47*, 4653.
- [37] S. Holliday, R. S. Ashraf, A. Wadsworth, D. Baran, S. A. Yousaf, C. B. Nielsen, C.-H. Tan, S. D. Dimitrov, Z. Shang, N. Gasparini, M. Alamoudi, F. Laquai, C. J. Brabec, A. Salleo, J. R. Durrant, I. McCulloch, *Nat. Commun.* **2016**, *7*, 11585.
- [38] S. F. Hoefler, T. Rath, N. Pastukhova, E. Pavlica, D. Scheunemann, S. Wilken, B. Kunert, R. Resel, M. Hobisch, S. Xiao, G. Bratina, G. Trimmel, *J. Mater. Chem. A* **2018**, *6*, 9506.
- [39] L. Huo, S. Zhang, X. Guo, F. Xu, Y. Li, J. Hou, *Angew. Chem., Int. Ed.* **2011**, *50*, 9697.
- [40] Y. Lin, F. Zhao, Q. He, L. Huo, Y. Wu, T. C. Parker, W. Ma, Y. Sun, C. Wang, D. Zhu, A. J. Heeger, S. R. Marder, X. Zhan, *J. Am. Chem. Soc.* **2016**, *138*, 4955.
- [41] Q. Wu, D. Zhao, A. M. Schneider, W. Chen, L. Yu, *J. Am. Chem. Soc.* **2016**, *138*, 7248.
- [42] Y. Zhong, M. T. Trinh, R. Chen, G. E. Purdum, P. P. Khlyabich, M. Sezen, S. Oh, H. Zhu, B. Fowler, B. Zhang, W. Wang, C.-Y. Nam, M. Y. Sfeir, C. T. Black, M. L. Steigerwald, Y.-L. Loo, F. Ng, X.-Y. Zhu, C. Nuckolls, *Nat. Commun.* **2015**, *6*, 8242.
- [43] J. Sun, Z. Zhang, X. Yin, J. Zhou, L. Yang, R. Geng, F. Zhang, R. Zhu, J. Yu, W. Tang, *J. Mater. Chem. A* **2018**, *6*, 2549.
- [44] D. Baran, T. Kirchartz, S. Wheeler, S. Dimitrov, M. Abdelsamie, J. Gorman, R. S. Ashraf, S. Holliday, A. Wadsworth, N. Gasparini,

- P. Kaienburg, H. Yan, A. Amassian, C. J. Brabec, J. R. Durrant, I. McCulloch, *Energy Environ. Sci.* **2016**, *9*, 3783.
- [45] S. Chen, Y. Liu, L. Zhang, P. C. Y. Chow, Z. Wang, G. Zhang, W. Ma, H. Yan, *J. Am. Chem. Soc.* **2017**, *139*, 6298.
- [46] D. Baran, R. S. Ashraf, D. A. Hanifi, M. Abdelsamie, N. Gasparini, J. A. Röhr, S. Holliday, A. Wadsworth, S. Lockett, M. Neophytou, C. J. M. Emmott, J. Nelson, C. J. Brabec, A. Amassian, A. Salleo, T. Kirchartz, J. R. Durrant, I. McCulloch, *Nat. Mater.* **2017**, *16*, 363.
- [47] S.-C. Chen, Q. Zheng, Z. Yin, D. Cai, Y. Ma, *Org. Electron.* **2017**, *47*, 79.
- [48] Z. He, C. Zhong, X. Huang, W. Y. Wong, H. Wu, L. Chen, S. Su, Y. Cao, *Adv. Mater.* **2011**, *23*, 4636.
- [49] Y. Qin, Y. Chen, Y. Cui, S. Zhang, H. Yao, J. Huang, W. Li, Z. Zheng, J. Hou, *Adv. Mater.* **2017**, *29*, 1606340.
- [50] J. A. Bartelt, D. Lam, T. M. Burke, S. M. Sweetnam, M. D. McGehee, *Adv. Energy Mater.* **2015**, *5*, 1500577.
- [51] N. Suzuki, T. Fujita, K. Y. Amsharov, J. Ichikawa, *Chem. Commun.* **2016**, *52*, 12948.
- [52] K. Y. Amsharov, M. A. Kabdulov, M. Jansen, *Angew. Chem., Int. Ed.* **2012**, *51*, 4594.
- [53] K. Y. Amsharov, P. Merz, *J. Org. Chem.* **2012**, *77*, 5445.
- [54] O. Papaianina, K. Y. Amsharov, *Chem. Commun.* **2016**, *52*, 1505.
- [55] Y. Liu, J. Zhao, Z. Li, C. Mu, W. Ma, H. Hu, K. Jiang, H. Lin, H. Ade, H. Yan, *Nat. Commun.* **2014**, *5*, 5293.
- [56] S. Zhang, Y. Qin, J. Zhu, J. Hou, *Adv. Mater.* **2018**, *30*, 1800868.
- [57] W. Zhao, S. Li, H. Yao, S. Zhang, Y. Zhang, B. Yang, J. Hou, *J. Am. Chem. Soc.* **2017**, *139*, 7148.
- [58] H. Yao, Y. Cui, R. Yu, B. Gao, H. Zhang, J. Hou, *Angew. Chem., Int. Ed.* **2017**, *56*, 3045.
- [59] H. Li, Z. Xiao, L. Ding, J. Wang, *Sci. Bull.* **2018**, *63*, 340.
- [60] Y. Sun, J. H. Seo, C. J. Takacs, J. Seifert, A. J. Heeger, *Adv. Mater.* **2011**, *23*, 1679.